Title: Explaining the Elegant Dynamics of the Ultra-Relativistic Third Van Allen Radiation Belt

Authors: I.R. Mann[1], L.G. Ozeke[1], K.R. Murphy[1,2], S. G. Claudepierre[3], D. L. Turner[3], D .N. Baker[4], I.J. Rae[5], A. Kale[1], D.K. Milling[1], A.J. Boyd[6], H. E. Spence[6], G. D. Reeves[7], H. J. Singer[8], S. Dimitrakoudis[9], I. A. Daglis[9,10] and F. Honary[11]

Affiliations:

[1]Department of Physics, University of Alberta, Edmonton, AB, T6G 2G7. Canada.

[2]NASA Goddard Spaceflight Center, Code 674, Greenbelt, Maryland, MD 20771, USA.

[3]The Aerospace Corporation, Los Angeles, CA 90009, USA

[4]Laboratory for Atmospheric and Space Physics, University of Colorado, Boulder, CO 80309, USA

[5] Mullard Space Science Laboratory, University College London, Holmbury St. Mary, Dorking, Surrey, RH5 6NT, UK.

[6]Institute for the Study of Earth, Oceans, and Space, University of New Hampshire, Durham, NH 03824-3525, USA

[7]Space and Atmospheric Sciences, NIS-1, Los Alamos National Laboratory, Los Alamos, NM 87544, USA.

[8]Space Weather Prediction Center, NOAA, Boulder, Colorado, 80305, USA.

[9]National Observatory of Athens, Institute for Astronomy, Astrophysics, Space Applications and Remote Sensing GR-15236, Penteli, Greece.

[10]Section of Astrophysics, Astronomy and Mechanics, Department of Physics, University of Athens, Greece.

[11]Department of Physics, Lancaster University, Lancaster, U.K.

*Correspondence to: imann@ualberta.ca

Abstract:

Since the discovery of the Van Allen radiation belts over 50 years ago, an explanation for their complete dynamics has remained elusive. Especially challenging is understanding the recently discovered ultra-relativistic third electron radiation belt. Current theory asserts

that loss in the heart of the outer belt, essential to the formation of the third belt, must be controlled by high-frequency plasma wave-particle scattering into the atmosphere, via whistler mode chorus, plasmaspheric hiss, or electromagnetic ion cyclotron waves. However, this has failed to accurately reproduce the third belt. Using a data-driven, time-dependent specification of ultra-low frequency (ULF) waves we show for the first time how the third radiation belt is established as a simple, elegant consequence of storm-time extremely fast outward ULF wave transport. High frequency wave-particle scattering loss into the atmosphere is not needed in this case. When rapid ULF wave transport coupled to a dynamic boundary is accurately specified, the sensitive dynamics controlling the enigmatic ultra-relativistic third radiation belt are naturally explained.

Text:

Introduction

Since their accidental discovery at the beginning of the space race [1], the processes responsible for the dynamics of the relativistic (>~ 500 keV) and ultra-relativistic (>~ 2MeV) electron populations in the Earth's Van Allen radiation belts have been hotly debated [2, 3]. It is generally understood that the belt dynamics arise from a delicate balance between acceleration, transport, and loss [4], with some recent modern studies highlighting a potential importance for high frequency wave-particle interactions [5, 6] over traditional radial transport [7] or ultra-low frequency (ULF) wave-particle resonance [8] for relativistic electron acceleration in the inner magnetosphere[9]. Concerning loss, in the main phase of geomagnetic storms, a puzzling and poorly understood rapid loss is often observed deep in the heart of the radiation belt, see e.g., the review by Turner et al. [10], followed by a replenishment of relativistic electron flux in the form of a distinct newly accelerated population. The recent discovery of an unexpected and puzzling

third Van Allen belt [11], especially clear at ultra-relativistic energies, provides additional challenges and new opportunities for understanding the dominant processes controlling belt dynamics especially by employing data of unprecedented resolution available from the two NASA Van Allen Probes following their launch on 30 August 2012 [3].

Explaining the enigmatic third radiation belt requires electrons to be rapidly lost in the main phase of geomagnetic storms, either by rapid scattering into the atmosphere by high frequency plasma wave-particle interactions, or alternatively through rapid loss out through the magnetopause in a process termed magnetopause shadowing [12]. Up until now, neither of these processes has provided a satisfactory explanation although recent modelling excluding the effects of ULF wave transport has improved our understanding of the storm-time loss of electrons from the outer zone [13]. The standard paradigm concludes that at lower L-shells (e.g., around L~<4, where L is the equatorial crossing point of a dipole magnetic field in units of Earth radii) the particles must have been scattered into the atmosphere by high-frequency plasma waves such as whistler mode chorus, plasmaspheric hiss, or electromagnetic ion cyclotron (EMIC) waves [14, 15]. Although magnetopause shadowing losses can occur at high L-values [16], the magnetopause even when compressed is usually deemed to be too distant for electrons in the heart of the outer belt to be lost there on the timescale observed. Recently, Shprits et al.[17] concluded that radial diffusion was not sufficient to establish the ultra-relativistic third belt morphology, and determined that EMIC loss confined to narrow L-shells in the heart of the outer belt was required. However, as described by Usanova et al.[18], such EMIC waves alone cannot affect the core of the ultra-relativistic equatorial pitch angle distribution at large pitch angles (pitch angle is the angle between the particle velocity and the background magnetic field), so

EMIC waves alone are unlikely to explain the loss of particles at all pitch angles required for the formation of the third radiation belt. Here we present an explanation for dominant ultra-relativistic electron dynamics and the generation of the third radiation belt through extremely fast ULF wave transport; very strong and rapid ULF wave coupling between the flux at the outer boundary and the dynamics of the interior belt are revealed thereby also explaining the formation of the third belt. Despite being an extensive focus of prior research, no high frequency wave-particle interaction losses are needed in this case. Similar transport will contribute to ultra-relativistic energetic particle dynamics in other astrophysical plasma regimes which are perturbed by time-dependent magnetic fields, stellar winds and/or plasma flows.

Results

Figure 1 presents an overview of the characteristics of the solar wind, and the resulting response in near-Earth space for the month of September 2012. On 2nd September 2012, losses deep in the outer electron radiation resulted in the outer belt being split in two, subsequently producing a morphology consisting of three distinct belts reported by Baker et al. [11]. The period was associated with only a moderate geomagnetic storm (minimum Dst = −74 nT; Figure 1(a)), driven by an extended period of southward interplanetary magnetic field (IMF) during the storm main phase (Figure 1(d)) which preceded a period of repeated large solar wind dynamic pressure increases over the next several days. The dynamic pressure increases only arrived later during the storm, first impacting the Earth around 12 UT on 3rd September 2012 and continuing into the 6th September 2012. Throughout the storm the solar wind speed remained relatively modest and only rose to exceed 500 kms^{-1} for a brief interval. The compression of the magnetosphere was seen by the GOES satellites at geosynchronous altitudes (Figure 1(f)), increasing the magnitude

of the dayside magnetic field well above the typical value of ~100 nT, and decreasing it on the nightside due to significant stretching of the magnetotail. This was accompanied by a strong compression of the Shue et al. [19] model subsolar magnetopause location to L~6 (Figure 1(e)) around 12 UT on 3rd September.

Figure 1(g) shows the ultra-relativistic radiation belt response of the omni-directional 3.4 MeV energy differential flux as measured by Relativistic Electron Proton Telescope (REPT) [20], part of the Energetic, Composition and Thermal (ECT) instrument suite [21] on-board Probe A from the NASA Van Allen Probes mission [3]. This panel shows how the ultra-relativistic outer radiation belt becomes split into two separate zones, as described but not explained by Baker et al. [11], with a long-lived isolated "storage ring" left as the remnant of the outer zone before a new but distinct outer belt is reformed at higher altitudes. These two distinct outer electron belts, and the more stable inner zone dominated by energetic ions [22], form a three-belt morphology. The feature of the isolated storage ring [11] at the inner edge of the outer zone then decays only very gradually over a period of around 20 days or more as a result of slow losses due to plasmaspheric hiss [23]. Significantly, the loss observed at the start of the storm occurs in the heart of the outer zone, reaches inwards to radial distances of L<4 , and is associated with a long interval of almost continuous strongly southward IMF. Later after around 12 UT on 3rd September is there a large increase in solar wind dynamic pressure (Pdyn) which results in compression of the Shue et al. model magnetopause to around L=6 and further radiation belt losses to L < 3.5. Nonetheless, even after the impact of the enhanced solar wind dynamic pressure a large distance remains between the Shue et al. model magnetopause location and the inward extent of the loss in the heart of the Van Allen belt. This large distance to the magnetopause, which during the losses on

the 2nd September remained at L >= 9, might lead one to naively conclude that the magnetopause does not therefore play a role in the loss. However, as we show here, extremely fast outward radial transport to the magnetopause enabled by ultra-low frequency (ULF) waves actually cause this near-Earth loss and is ultimately fundamental to the generation of the third belt.

ULF waves have long been hypothesized to be responsible for the radial transport of relativistic electrons through work done on them by the fields and which causes them to move inward (or outward) as they are accelerated (or decelerated) [24-27]. Stochastically, depending on the local gradient of the phase space density, the net result is an inward [28] or outward [16, 29, 30] radial diffusive transport. The rates of ULF wave driven radial diffusion are characterized through a diffusion coefficient which is proportional to the perturbing ULF wave power. The details of the timescale of response of the belts to the diffusion equation (see for example [7, 25, 31]) depend on both the local phase space density gradient and the magnitude of the diffusion coefficient. For electric field diffusion, which dominates (see e.g., Ozeke et al. [25] and references therein), the diffusion coefficient scales as L^6 in a dipole field and is additionally proportional to the ULF wave power at the drift resonance frequency at the energy of the particles concerned. In the model presented here, observational characterization of ULF wave power as a function of L* multiplied by an electric diffusion coefficient with an assumed L^{*6} dependence is used to model the dynamics of ultra-relativistic electrons under the action of ULF wave diffusion.

ULF wave power is typically described using an empirical [28] or statistical [25, 26] relationship to a geomagnetic index such as Kp. However, by definition such averages neglect the extremes of the distribution. A more accurate representation of the transport can be obtained by using the

observed ULF wave power and this is the approach adopted here using data from the ground-based magnetometer stations listed in Supplementary Information Table 1 (available online). As shown in Extended Data Fig. 1 (available online), the ULF wave power during the main phase of this storm is at times orders of magnitude larger than that derived from statistical ULF wave power parameterizations as a function of activity indices derived from the whole solar cycle, and this can have an effect which is both fundamental and drastic.

Figures 2 and 3 show the impacts of using observed ULF wave power in our dynamical model of the ultra-relativistic radiation belt. Note that this model excludes any effects from local whistler mode chorus acceleration[32]. The radiation belt dynamics shown in Figure 2 and 3 were calculated using a one dimensional radial diffusion model as a function of the Roederer L* drift co-ordinate [33].The flux at constant energy is calculated from the phase space density from multiple first adiabatic invariant conserving radial diffusion simulations using conversion based on the L* and time-dependence of the Tsyganenko 04D magnetic field model interpolated to regular energy to generate flux at fixed energy channels for direct comparison with observations. The model is driven by an outer boundary condition at L*=5.25 comprising observed electron flux spectra and with radial transport driven by observed ULF wave power. The ULF wave electric field power, which drives the electron transport, is estimated using data from ground-based magnetometers and mapped from the ground through the ionosphere and into the equatorial plane electric field [34]. Since ULF wave power typically peaks in the dawn local time sector, mapping from the ground magnetometer stations to L* is completed in the 0600 magnetic local time (MLT) sector to impose the ULF transport in the model. The effects of plasma wave scattering into the atmosphere from plasmaspheric hiss and chorus waves, inside

and outside the plasmapause, are included (excluded) in the model output in the middle (bottom) panels of Figures 2 and 3 (see Supplementary Information, available online, for more details).

The differential flux at the outer boundary was specified using data from the REPT instrument. Note that during the loss interval, the lower energy magnetic electron spectrometer (MagEIS) on the Van Allen Probes had yet to be commissioned such that no MagEIS data is available to specify the outer boundary condition from Van Allen Probes data at lower energies. Note that particles in the MagEIS energy range do not significantly alter the flux above 3.4 MeV above L=2. Since loss from outward radial diffusion relies on an inward local gradient in phase space density, the value of the phase space density at the outer edge of the outer radiation belt is critical. Significantly, a period of low electron flux at the outer boundary plays a crucial role in the outward electron transport by ULF waves and results in the generation of the third radiation belt. In our simulation the outer boundary is assumed to be effectively devoid of flux as a result of loss through the magnetopause from 12UT on 2 September until it recovers at 15 UT on 5 September 2012 (see > 2 MeV geosynchronous GOES satellite data in Extended Data Fig. 2 available online) after which time the flux is again constrained by observations. The simulation is started at 12 UT on 1st September, with simulation results from 00 UT on September 2nd being shown in Figures 2 and 3 (further details of the methodology are provided in Supplementary Information available online).

Given that the range of observed ultra-relativistic differential fluxes spans four orders of magnitude the agreement between the absolute fluxes from the model and those observed by REPT shown in Figures 2 and 3 is excellent. At 3.4 MeV the storage ring produced by our model

is very distinct, has a sharp boundary like that seen in the data; however, there are some uncertainties in the mapping which should be used to transform the observed ground-based ULF wave power below L~4 into equatorial electric fields mostly because the mapping of wave power from the ground to space there is less well-constrained than at higher L (see also further discussion in the Supplementary Information available online). Nonetheless, the agreement at both energies is extremely good with the three belt structure being very clear. Importantly, in order for the third belt structure to be established, the ULF wave power needs to be strong enough (and penetrate sufficiently deeply) during a period when the outer boundary also remains devoid of flux. This interaction is rather sensitive such that refilling can sometimes merge the outer part of the belt with the remnant storage ring, and in that case only a two belt, rather than a three-belt, morphology results. As is abundantly clear in Figures 2 and 3, especially comparing the middle and bottom panels, neither chorus nor hiss waves are responsible for the third belt morphology although of course these losses can have a weak affect by generating some changes and specifically a slow decay of the flux [23]. Since EMIC wave effects are excluded in all model runs, they are not required to explain the generation of the third belt morphology either.

Extended Data Fig. 3 (available online) shows details of the electron phase space density profiles for nearly equatorially mirroring electrons observed by the Van Allen Probes with a first adiabatic invariant of 2500 MeV/G calculated using the method described by Boyd et al.[35]. As is clearly shown, the gradient of the phase density clearly reverses from the outward gradient before the storm, to containing a steep inward gradient during the period of the strong electron losses which is generated by ULF wave coupling to the low phase space density at the outer boundary. This demonstrates that enhanced ULF wave outward diffusion caused the loss of

particles down to at least L*~3.3 (this is discussed further in Supplementary Information available online). Following the losses, and the recovery of the flux at the outer boundary, ULF waves can then also cause inward transport, acceleration and refilling of the outer part of the outer zone as a result of inward ULF wave radial diffusion. The model results demonstrate that ULF wave acceleration and transport also reproduces the subsequent recovery of radiation belt fluxes in good agreement with observations. Note that the model results shown in Figures 2 and 3 do not include any effects from chorus wave acceleration. Moreover, across the L* values sampled by the Van Allen Probes and at the value of the first invariant shown in Extended Data Fig. 3, there is also no evidence of a locally growing peak in phase space density such as that observed by Reeves et al. [6] which would be expected to accompany local chorus wave acceleration. Similar behavior, and phase space density gradient reversals without local peaks are also seen in higher first invariants up to at least 4000 MeV/G (not shown).

Fast ULF Wave Outward Radial Diffusion

Overall our results show that both the dynamical variation of the outer boundary condition and the strength of storm-time ULF wave power are very important for accurately characterizing radiation belt dynamics and for establishing a third belt. This can be understood in terms of the consequences of the magnetospheric impact of the leading edge of the solar wind drivers. The southward IMF and compression, arising from the impact of interplanetary coronal mass ejections or fast solar wind stream interfaces, erode the magnetopause through dayside magnetic reconnection and further compress the magnetopause inwards. However, as described for example by Hudson et al. [14], the magnetopause location does not typically reach the inner magnetosphere. Indeed in the case presented here, very significant loss occurs in the early part of

the storm and in advance of the impact of the strong dynamic pressure pulses and the resulting magnetopause compression to lower L. Significantly, such solar wind drivers produce very large amplitude ULF waves[27] and hence can generate extremely fast outward radial transport to even a relatively distant magnetopause, leaving only a small remnant belt (i.e., the "storage ring"). Together with subsequent replenishment of the outer parts of the belt, which does not reach the storage ring, this naturally explains the production of the three belt structure. Fast ULF wave transport may also explain the correlation between the locus of the superposed model magnetopause location and the locus of the outer edge of the outer zone radiation belt seen in GPS satellite energetic electron count rates for sudden impulse events reported by Morley et al.[36], even though they were separated by ~3-4 L-shells.

The process of extremely fast ULF wave transport, loss through the magnetopause, and subsequent recovery is shown schematically in Figure 4. All prior studies to our knowledge, even those in sophisticated 3-D models such as VERB [37], the British Antarctic Survey (BAS) Radiation Belt mode [38], and Salammbo [9], have used either empirical radial diffusion coefficients such as presented by Brautigam and Albert [28], or solar-cycle statistical dependences of ULF wave power on geomagnetic indices to drive diffusion. All of these under-estimate the actual intense ULF wave power during the storm main phase, and therefore at such times these empirical representations probably should not be used to model the response of the belts (cf. Extended Data Fig. 1 available online). Such approaches naturally draw the conclusion, such as presented by reference [39], that "*depletion of the main phase relativistic electron fluxes at* $L \leq 4$ *can not be explained only by variations in fluxes near geosynchronous orbit*". In contrast, our results show that at ultra-relativistic energies using observed ULF wave power can generate

sufficiently fast outward radial transport across the magnetopause to cause main phase loss leading to a three radiation belt morphology. In future, these models could be run using improved ULF wave-driven diffusion coefficients coupled to an accurately specified dynamic outer boundary condition to further validate their impact on three-dimensional belt morphology.

As shown in Figures 2 and 3, at least when the outer boundary flux is constrained at L*=5.25, then the recovery of flux in the outer part of the belts can also be explained in our model by the inwards radial transport of a lower energy source population by ULF waves; no local acceleration from chorus waves at L*<5.25 is required. Of course, the processes which explain the temporal dynamics of the source population at the edge of our simulation are not examined here and remain very important. This includes coupling to the plasmasheet, and could also include the effects from local chorus wave accelerated sources outside the simulation domain examined here at L*>=5.25. So long as this ULF transport is sufficiently fast, the third belt morphology can be generated by a wide range of absolute ULF wave power so long as this enhanced power reaches the sufficiently low-L (see e.g., Extended Data Figures 4 and 5 and the additional discussion in the Supplementary Information available online).

Previous attempts to explain the ultra-relativistic third belt have resorted to the inclusion of high frequency plasma wave scattering loss into the atmosphere from closed magnetic field lines in the heart of the outer belt. For example, Shprits et al. [17] required a narrow region of "*scattering by electromagnetic ion cyclotron waves to the Earth's atmosphere*" to explain the loss needed to establish the third belt in their model. However, as discussed by Usanova et al.[18] such EMIC wave losses alone cannot affect the core of the ultra-relativistic electron distribution. Indeed,

with an accurate characterization of ULF wave transport coupled to a dynamic outer boundary, our results show clearly that such high frequency plasma wave effects are not needed to establish the three-belt morphology observed in September 2012 and reported by Baker et al..[11] Shprits et al. [17] used radial diffusion coefficients defined by Brautigam and Albert [28] - but as shown clearly in Extended Data Fig. 1, this may fail to accurately represent the actual ULF wave transport. Moreover, as we have shown here, coupling to a correct specification of the time-dependence of the source population at the outer boundary is also of critical importance. Together, these are likely the reason why prior studies of ultra-relativistic belt dynamics have required the inclusion of complex high frequency wave-particle interactions to try to explain the generation of the enigmatic third belt. For this storm, the minimum Dst is moderate and hence the Dst-effect cannot explain the required loss at low-L either (see Extended Data Figure 6 and the discussion in Supplementary Information which is available online).

Elegant Ultra-Relativistic Belt Dynamics

Occam's razor states that "*Entities should not be multiplied beyond necessity*" [40] while Sir. Isaac Newton offered in Rule Number 1 of his Rules of Reasoning in Philosophy that "*We are to admit no more causes of natural things than such as are both true and sufficient to explain their appearances*" [41]. Both of these apply to the generation of the structure of the ultra-relativistic third radiation belt. Unlike at lower energies (see e.g., Glauert et al.[38] at around 1 MeV), for ultra-relativistic electrons the complexities of high frequency plasma wave atmospheric scattering from chorus, hiss, or EMIC waves are not required to define the dominant belt morphology at least in this case. Once the correct ULF wave physics is included the generation and dynamics of the ultra-relativistic third radiation belt are seen to arise as a natural, simple and

elegant consequence of the action of properly quantified ULF wave electron transport coupled to a dynamic outer boundary condition.

References.

1. Van Allen, J. A. & Frank, L. A. Radiation around the Earth to a radial distance of 107,400 km. Nature 183, 430 - 434 (1959).

2. Friedel, R., Reeves, G. & Obara, T. Relativistic electron dynamics in the inner magnetosphere—A review. J. Atmos. Solar Terr. Phys. 64, 265-282 (2002).

3. Kessel, R., Fox, N. & Weiss, M. The radiation belt storm probes (RBSP) and space weather. Space Science Reviews 179, 531-543 (2013).

4. Reeves, G., McAdams, K., Friedel, R. & O'Brien, T. Acceleration and loss of relativistic electrons during geomagnetic storms. Geophys. Res. Lett. 30, doi: 10.1029/2002GL016513 (2003).

5. Chen, Y., Reeves, G. D. & Friedel, R. H. The energization of relativistic electrons in the outer Van Allen radiation belt. Nature Physics 3, 614-617 (2007).

6. Reeves, G. D. et al. Electron acceleration in the heart of the Van Allen radiation belts. Science 341, 991-994 (2013).

7. Schulz, M. & Lanzerotti, L. J. in Particle diffusion in the radiation belts (Springer, Berlin, 1974).

8. Mann, I. R. et al. Discovery of the action of a geophysical synchrotron in the Earth's Van Allen radiation belts. Nature communications 4, doi:10.1038/ncomms3795 (2013).

9. Varotsou, A. et al. Simulation of the outer radiation belt electrons near geosynchronous orbit including both radial diffusion and resonant interaction with whistler-mode chorus waves. Geophys. Res. Lett. 32, doi: 10.1029/2005GL023282 (2005).

10. Turner, D., Morley, S., Miyoshi, Y., Ni, B. & Huang, C. in Dynamics of the Earth's radiation belts and inner magnetosphere 195-212 (Wiley, Washington, DC, 2012).

11. Baker, D. N. et al. A long-lived relativistic electron storage ring embedded in Earth's outer Van Allen belt. Science 340, 186-190 (2013).

12. Loto'aniu, T. et al. Relativistic electron loss due to ultralow frequency waves and enhanced outward radial diffusion. J. Geophys. Res. 115, doi: 10.1029/2010JA015755 (2010).

13. Ukhorskiy, A. et al. Global storm time depletion of the outer electron belt. J. Geophys. Res., 120, 2543–2556, doi:10.1002/2014JA020645 (2015).

14. Hudson, M. et al. Simulated magnetopause losses and Van Allen Probe flux dropouts. Geophys. Res. Lett. 41, 1113-1118 (2014).

15. Yu, Y., Koller, J. & Morley, S. Quantifying the effect of magnetopause shadowing on electron radiation belt dropouts. Ann. Geophys. 31, 1929-1939 (2013).

16. Turner, D. L., Shprits, Y., Hartinger, M. & Angelopoulos, V. Explaining sudden losses of outer radiation belt electrons during geomagnetic storms. Nature Physics 8, 208-212 (2012).

17. Shprits, Y. Y. et al. Unusual stable trapping of the ultrarelativistic electrons in the Van Allen radiation belts. Nature Physics 9, 699–703 (2013).

18. Usanova, M. et al. Effect of EMIC waves on relativistic and ultrarelativistic electron populations: Ground-based and Van Allen Probes observations. Geophys. Res. Lett. 41, 1375-1381 (2014).

19. Shue, J. et al. Magnetopause location under extreme solar wind conditions. J. Geophys. Res. 103, 17691-17700 (1998).

20. Baker, D. et al. in The Van Allen Probes Mission 337-381 (Springer, New York, 2014).

21. Spence, H. E. et al. in The Van Allen Probes Mission 311-336 (Springer, New York, 2014).

22. Fennell, J. et al. Van Allen Probes show that the inner radiation zone contains no MeV electrons: ECT/MagEIS data. Geophys. Res. Lett. 42, 1283 (2015).

23. Thorne, R. et al. Evolution and slow decay of an unusual narrow ring of relativistic electrons near L~ 3.2 following the September 2012 magnetic storm. Geophys. Res. Lett. 40, 3507-3511 (2013).

24. Elkington, S. R., Hudson, M. K. & Chan, A. A. Resonant acceleration and diffusion of outer zone electrons in an asymmetric geomagnetic field. J. Geophys. Res. 108, 1116 (2003).

25. Ozeke, L. G. et al. ULF wave derived radiation belt radial diffusion coefficients. J. Geophys. Res. 117, doi: 10.1029/2011JA017463 (2012).

26. Ozeke, L. G., Mann, I. R., Murphy, K. R., Jonathan Rae, I. & Milling, D. K. Analytic expressions for ULF wave radiation belt radial diffusion coefficients. J. Geophys. Res. 119, 1587-1605 (2014).

27. Mann, I. R. et al. in Dynamics of the Earth's Radiation Belts and Inner Magnetosphere 69-92 (Wiley, New York, 2012).

28. Brautigam, D. & Albert, J. Radial diffusion analysis of outer radiation belt electrons during the October 9, 1990, magnetic storm. J. Geophys. Res. 105, 291-309 (2000).

29. Loto'aniu, T. et al. Radial diffusion of relativistic electrons into the radiation belt slot region during the 2003 Halloween geomagnetic storms. J. Geophys. Res. 111, doi: 10.1029/2005JA011355 (2006).

30. Shprits, Y. et al. Outward radial diffusion driven by losses at magnetopause. Journal of Geophysical Research: Space Physics (1978--2012) 111 (2006).

31. Brizard, A. J. & Chan, A. A. Relativistic bounce-averaged quasilinear diffusion equation for low-frequency electromagnetic fluctuations. Phys. Plasmas 8, 4762-4771 (2001).

32. Li, W and Thorne, RM and Ma, Q and Ni, B and Bortnik, J and Baker, DN and Spence, Harlan E and Reeves, GD and Kanekal, SG and Green, JC and others. Radiation belt electron acceleration by chorus waves during the 17 March 2013 storm. Journal of Geophysical Research: Space Physics 119, 4681-4693 (2014).

33. Roederer, J. G. in Dynamics of geomagnetically trapped radiation (Springer, New York, 1970).

34. Ozeke, L., Mann, I. & Rae, I. Mapping guided Alfven wave magnetic field amplitudes observed on the ground to equatorial electric field amplitudes in space. J. Geophys. Res. 114 (2009).

35. Boyd, A. et al. Quantifying the radiation belt seed population in the 17 March 2013 electron acceleration event. Geophys. Res. Lett. 41, 2275-2281 (2014).

36. Morley, S. K. et al. Dropouts of the outer electron radiation belt in response to solar wind stream interfaces: global positioning system observations. Proc. Roy. Soc. A, rspa20100078 (2010).

37. Shprits, Y. Y., Subbotin, D. & Ni, B. Evolution of electron fluxes in the outer radiation belt computed with the VERB code. J. Geophys. Res. 114, doi: 10.1029/2008JA013784 (2009).

38. Glauert, S. A., Horne, R. B. & Meredith, N. P. Three-dimensional electron radiation belt simulations using the BAS Radiation Belt Model with new diffusion models for chorus, plasmaspheric hiss, and lightning-generated whistlers. J. Geophys. Res. 119, 268-289 (2014).

39. Shprits, Y. & Thorne, R. Time dependent radial diffusion modeling of relativistic electrons with realistic loss rates. Geophys. Res. Lett. 31 (2004).

40. Tornay, S. C. in Ockham: Studies and Selections (Open Court Publishers, La Salle, IL, 1938).

41. Newton, I. in Newton’s Principia: Motte’s Translation revisited. Sir Isaac Newton's mathematical principles of natural philosophy and his system of the world (Univ of California Press., Los Angeles, 1934).

Supplementary Information is linked to the online version of the paper at www.nature.com/nphys

Acknowledgments:

CARISMA data is available from www.carisma.ca, other magnetometer data from SAMNET and IMAGE and from the SuperMAG program at supermag.jhuapl.edu, REPT data from www.rbsp-ect.lanl.gov, solar wind, GOES data from http://satdat.ngdc.noaa.gov/sem/goes/data/new_full/, THEMIS data from cdaweb.gsfc.nasa.gov, and geomagnetic indices from wdc.kugi.kyoto-u.ac.jp. IRM is supported by a Discovery Grant from Canadian NSERC. IJR is funded by STFC grant ST/L000563/1 and NERC grant NE/L007495/1. KRM is supported by an NSERC Postdoctoral Fellowship. CARISMA is operated by the University of Alberta, funded by the Canadian Space Agency. We acknowledge the WDC for Geomagnetism, Kyoto University, Japan for the geomagnetic indices. We acknowledge NASA contract NAS5-02099 and V. Angelopoulos for use of data from the THEMIS Mission. Specifically D. Larson and R. P. Lin for use of SST data and C. W. Carlson and J. P. McFadden for use of ESA data. We thank A. Kellerman and T. Onsager for helpful discussions. This work was supported by RBSP-ECT funding provided by JHU/APL Contract No. 967399 under NASA's Prime Contract No. NAS5-01072. The Sub-Auroral Magnetometer Network (SAMNET) is operated by the Space Plasma Environment and Radio Science (SPEARS) group, Department of Physics, Lancaster University. We thank the institutes who maintain the IMAGE Magnetometer Array. This work was supported in part by participation in the MAARBLE (Monitoring, Analyzing and Assessing Radiation Belt Loss and Energization) consortium. MAARBLE has received funding from the European Community's Seventh Framework Programme (FP7-SPACE-2010-1, SP1 Cooperation, Collaborative project) under grant agreement n° 284520. This paper reflects only the authors' views and the European Union is not liable for any use that may be made of the information contained herein.

Author Contributions: IRM wrote the manuscript and provided leadership for the project; LGO completed all of the simulation work, including incorporation of observational data into the boundary conditions and incorporating the specifications of empirical loss; KRM and IJR analyzed the CARISMA ULF wave data, DT provided analysis support for the THEMIS data, HJS for the GOES data, and SC, DB and AB for the REPT data, DKM supported interpretation of the CARISMA data, SD and ID analysed supporting storm-time ULF wave statistics, GR and HS provided ECT project leadership, FH SAMNET data, and AK developed Figure 4. All authors contributed to editing the final manuscript.

Author information:

The authors declare no competing financial interests.

Correspondence and requests for information should be send to imann@ualberta.ca

Figure Legends

Figure 1. Overview of driving solar wind and magnetospheric response during the generation of the third radiation belt. Storm-time disturbance index (Dst), solar wind speed, dynamic pressure, and inter-planetary magnetic field (GSE z-component) (panels (a-d)); model magnetopause location from Shue et al. (panel (e)); Hp magnetic field component observed by GOES East (red) and West (blue) (panel (f)); and the 3.4 MeV electron flux observed by the REPT instrument on Van Allen Probe A (panel (g)) for the month of September 2012. The third ultra-relativistic Van Allen belt is clearly seen in the bottom panel.

Figure 2. Comparison between observed and modelled period of third radiation belt generation at 3.4 MeV. Observed (top) and modeled (bottom two panels) spin averaged electron flux as a function of L* from 2-15th September 2012. The middle panels shows the simulation run including not only ULF wave inward and outward radial diffusion, but also models for the Kp-dependent chorus and hiss loss inside and outside the plasmaspause, respectively (see Supplementary Information available online for details). The bottom panel shows a simulation results with only inward and outward ULF wave transport, acceleration and loss, and with all high frequency chorus and hiss wave-particle losses switched off. The model also does not include any effects from chorus wave acceleration or EMIC wave loss.

Figure 3. Comparison between observed and modelled period of third radiation belt generation at 5.2 MeV. Same format as Figure 2.

Figure 4. Schematic of the time series of the processes generating the third radiation belt. (a) Solar wind drivers including southward IMF followed by solar wind compression impact the magnetosphere at the start of the storm with a pre-existing two radiation belt structure comprising a single outer (purple) and inner (green) belt; (b) intense ULF waves drive extremely fast outwards radial diffusion and loss from the heart of the outer radiation belt; (c) a remnant storage ring at the inner edge of the outer zone remains; (d) the outer parts of the belts are replenished to form a new distinct additional belt at higher L-shells.

Figures

Figure 1

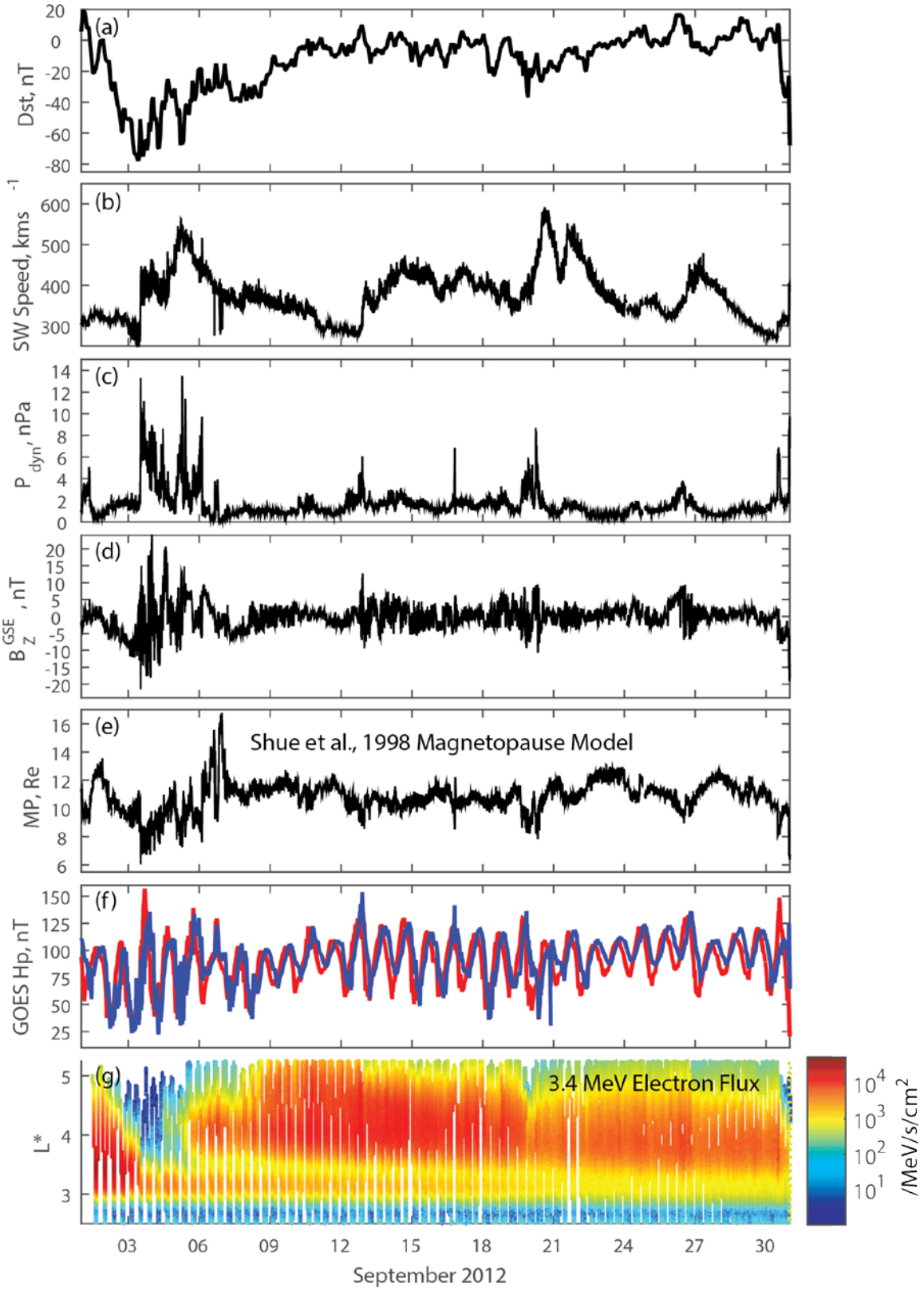

Figure 2.

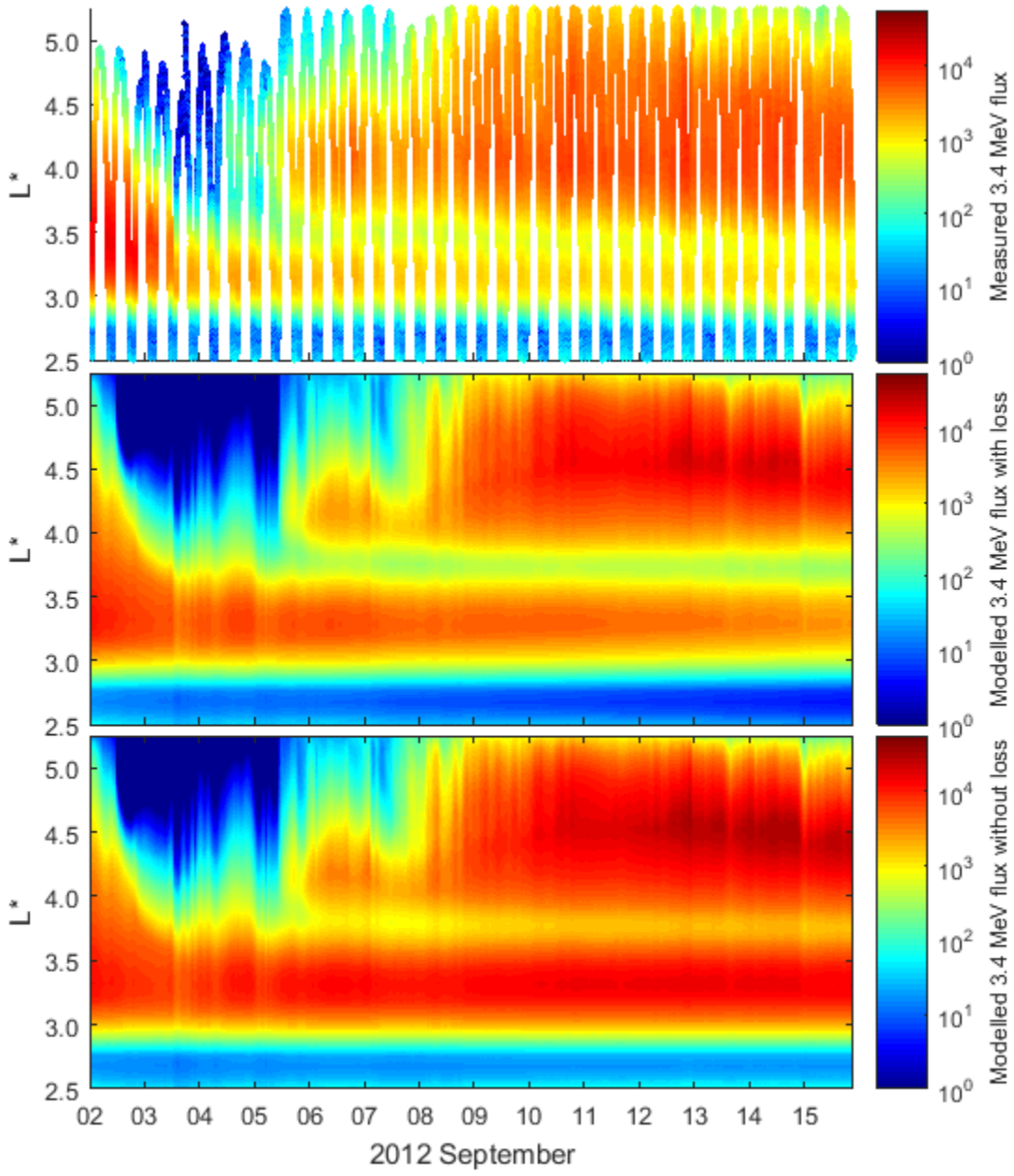
L*
5.0
4.5
4.0
3.5
3.0
2.5
02
03
04
05
06
07
08
09
10
11
12
13
14
15
2012 September
10^4
10^3
10^2
10^1
10^0
Measured 3.4 MeV flux
Modelled 3.4 MeV flux with loss
Modelled 3.4 MeV flux without loss

Figure 3.

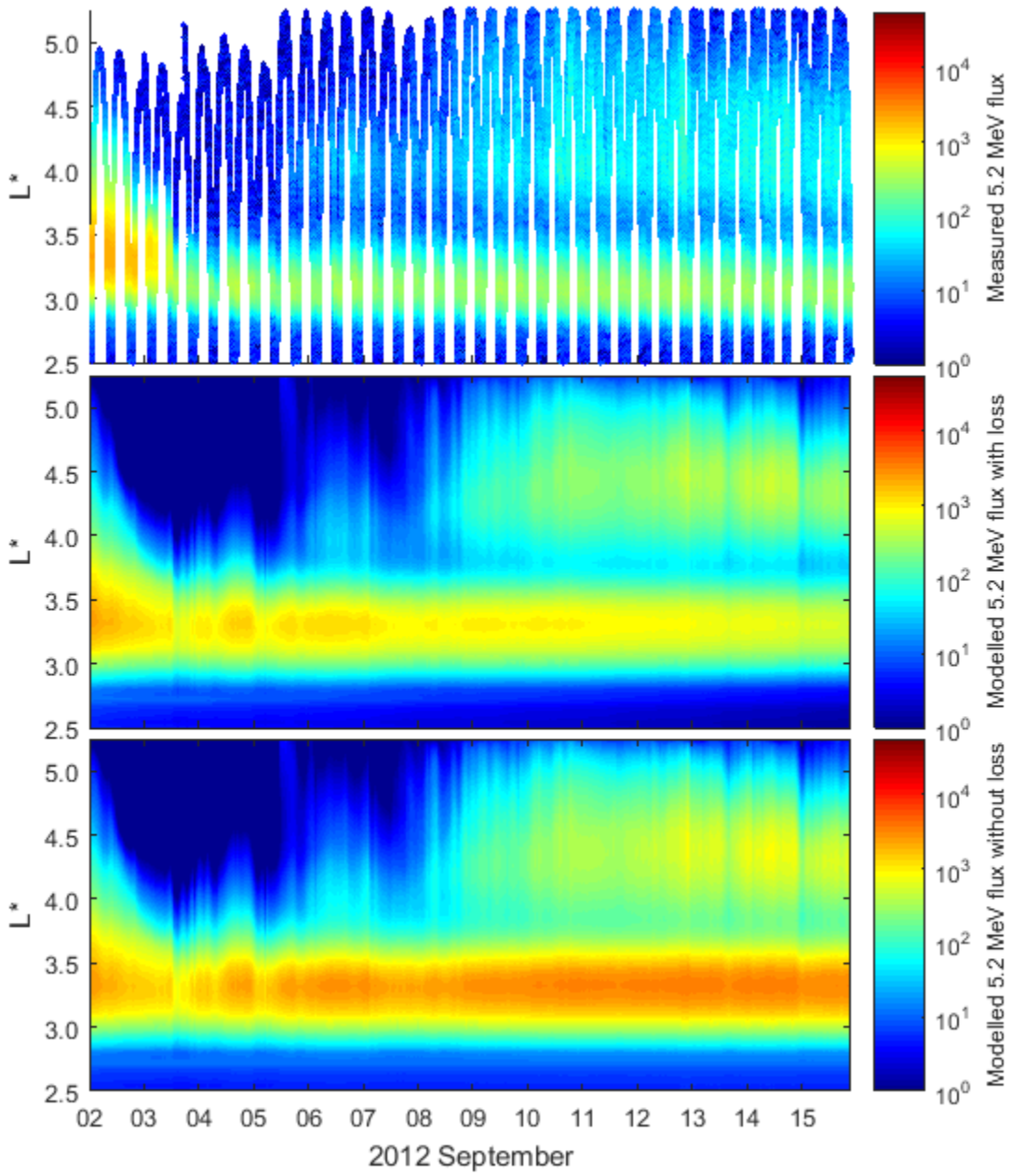
L*
5.0
4.5
4.0
3.5
3.0
2.5
Measured 5.2 MeV flux
Modelled 5.2 MeV flux with loss
Modelled 5.2 MeV flux without loss
10^0
10^1
10^2
10^3
10^4
02 03 04 05 06 07 08 09 10 11 12 13 14 15
2012 September

Figure 4.

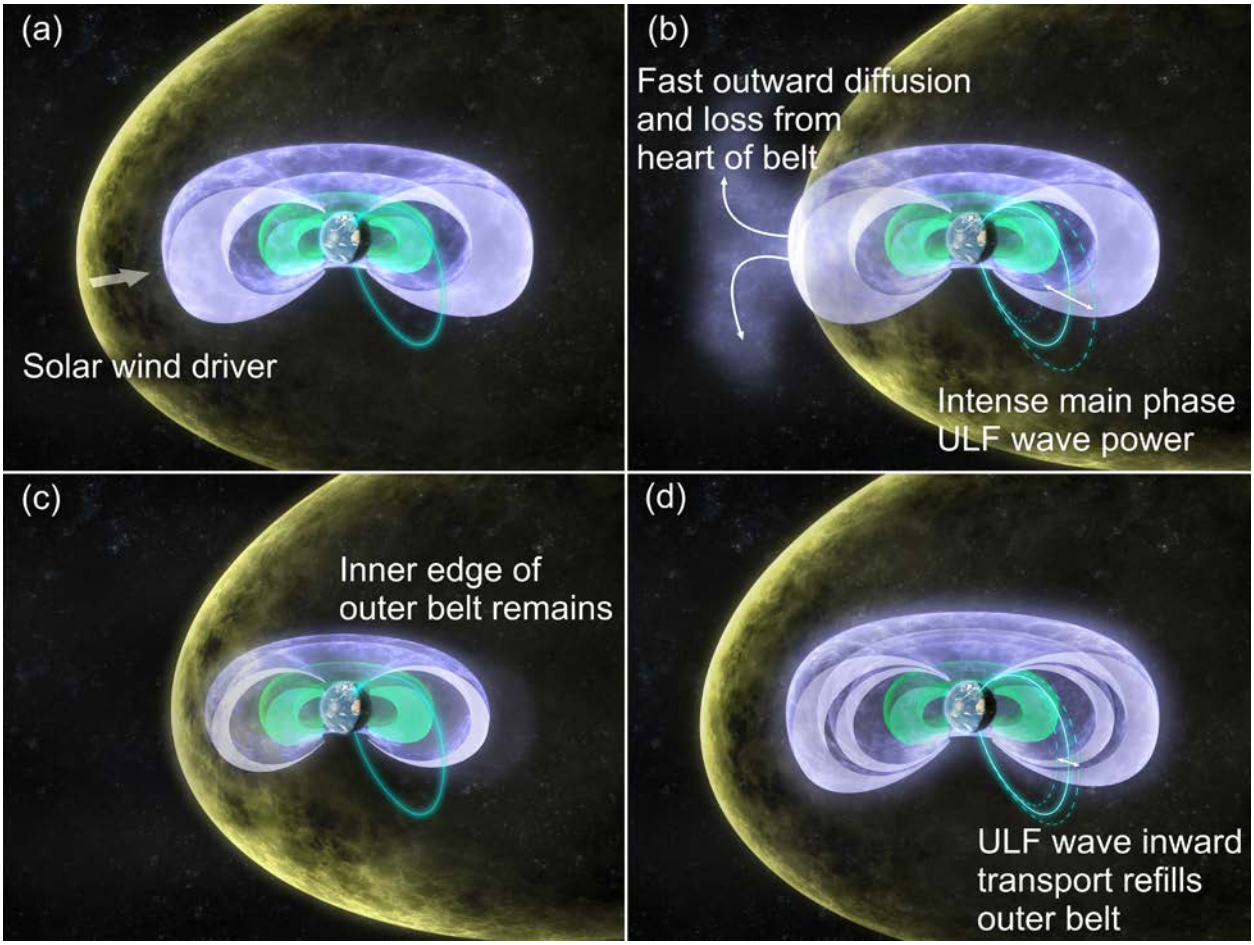
(a)
Solar wind driver
(b)
Fast outward diffusion
and loss from
heart of belt
Intense main phase
ULF wave power
(c)
Inner edge of
outer belt remains
(d)
ULF wave inward
transport refills
outer belt

Extended Data.

Extended Data Figure 1.

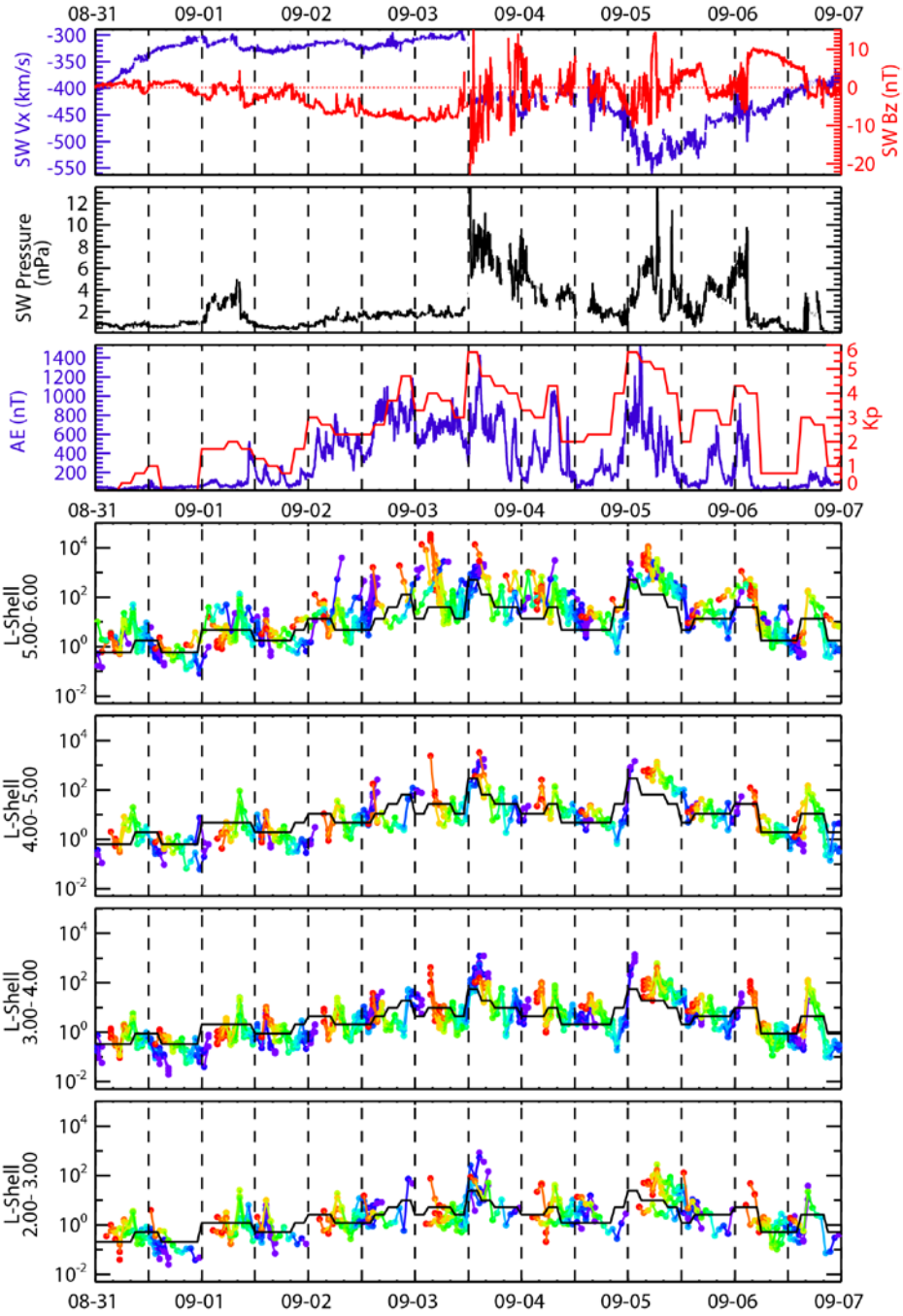

Extended Data Fig. 1. Driving solar wind, geomagnetic activity and ULF wave response. Solar wind speed along the sun-Earth line (blue) and GSM z-component of the interplanetary magnetic field (red) (top); solar wind dynamic pressure (second panel); Auroral Electrojet index (AE; blue) and planetary K-index (Kp; red) (third panel). Observed integrated 1-10mHz ULF wave power inside the magnetosphere (log scale) gathered from global ground-based magnetometer

observations (last four panels): each panel shows data from a specific L-shell range, with colour (on a scale from red-green-purple) indicating the dayside MLT from 06-18MLT of the observing station; solid line shows the solar cycle statistical ULF power based on Kp for the middle of each L-shell range. Clearly the observed ULF wave power exceeds the statistical values during this period, especially during the period of generation of the third radiation belt.

Extended Data Figure 2

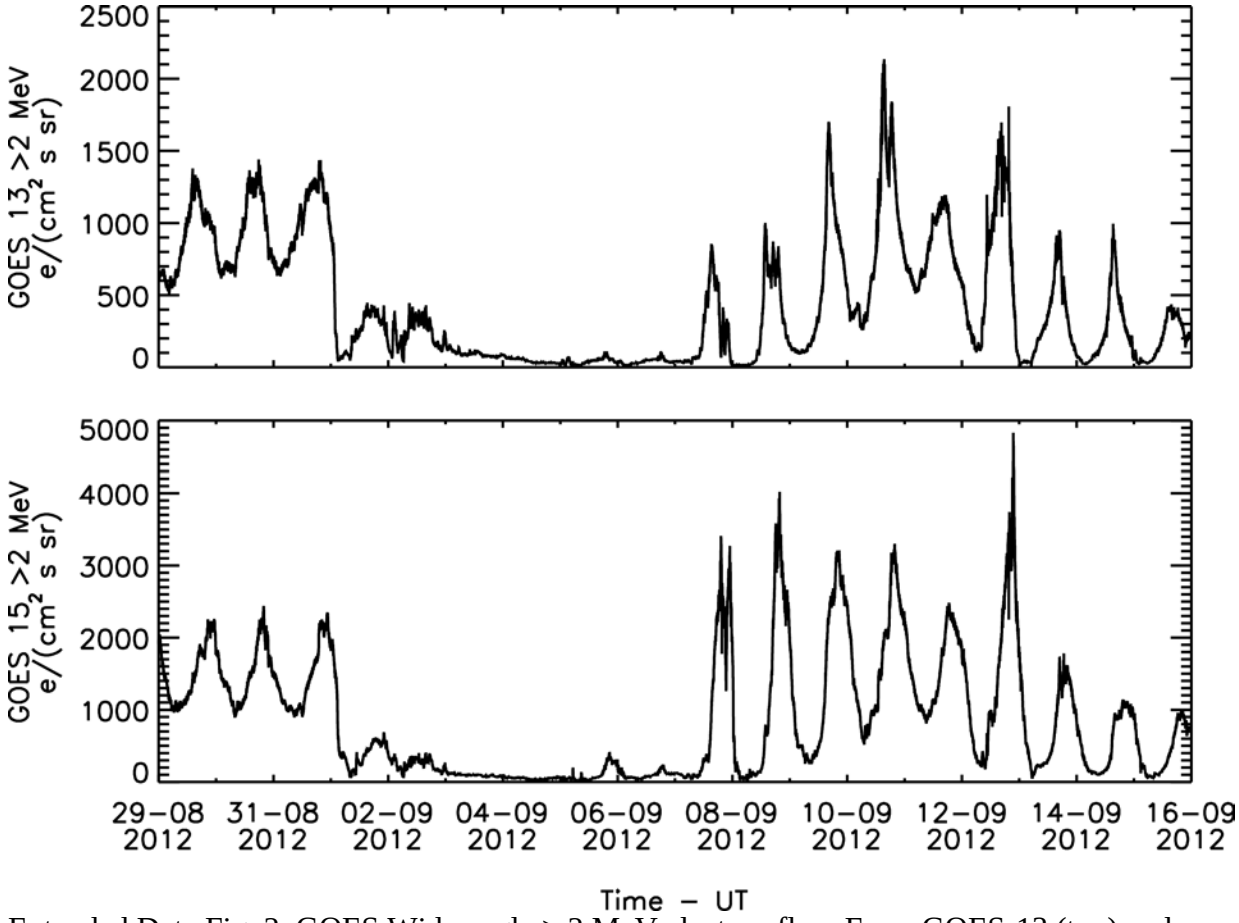

Extended Data Fig. 2. GOES Wide angle > 2 MeV electron flux. From GOES-13 (top) and GOES-15 (bottom).

Extended Data Figure 3

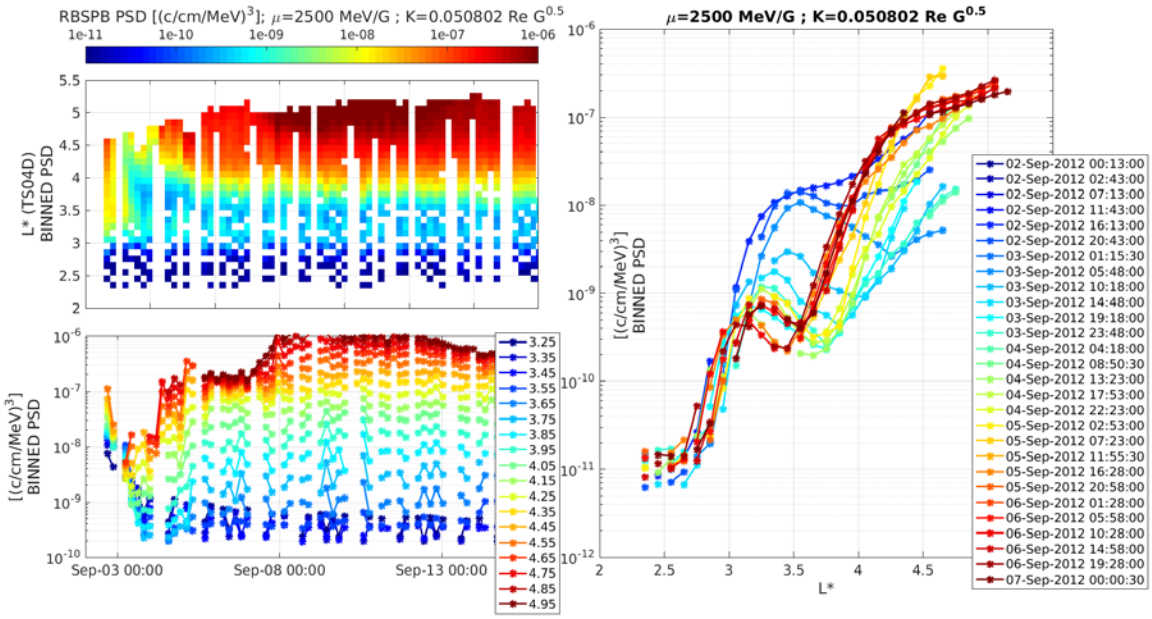

Extended Data Fig. 3. Observed profiles of electron phase space density as a function of L*. Profiles of the phase space density (PSD) of electrons with first adiabatic invariant of 2500 MeV/G and near 90 degree pitch angle (second invariant K = 0.051 Re $G^{0.5}$) as a function of L* as observed by the Van Allen Probes: (top left) PSD as a function of binned L*, (bottom left) phase space density as a color coded function L*, the ranges of L* being shown in the legend. (right panel) Time slices of electron phase space density as a function of L* from a series of Van Allen Probe passes from the dates and times shown in the legend. A clear reversal from an outwards to a steep inward radial gradient of phase space density is seen during the loss interval. This outward PSD gradient reaches L*~3.3,the profiles being consistent with extremely fast outward diffusion driven by ULF waves coupled to strongly reduced flux at the outer boundary driving losses which reach the heart of the outer belt. The subsequent recovery of the outer parts of the outer zone are consistent with renewed inward transport following the recovery of the flux at the outer edge of the belt (days colour coded approximately yellow through red in the right-hand panel). The decay of the phase space density peak at L*~3.3 is consistent with the slow decay of the third belt morphology due to the gradual scattering of electrons into the atmosphere by plasmaspheric hiss.

Extended Data Figure 4

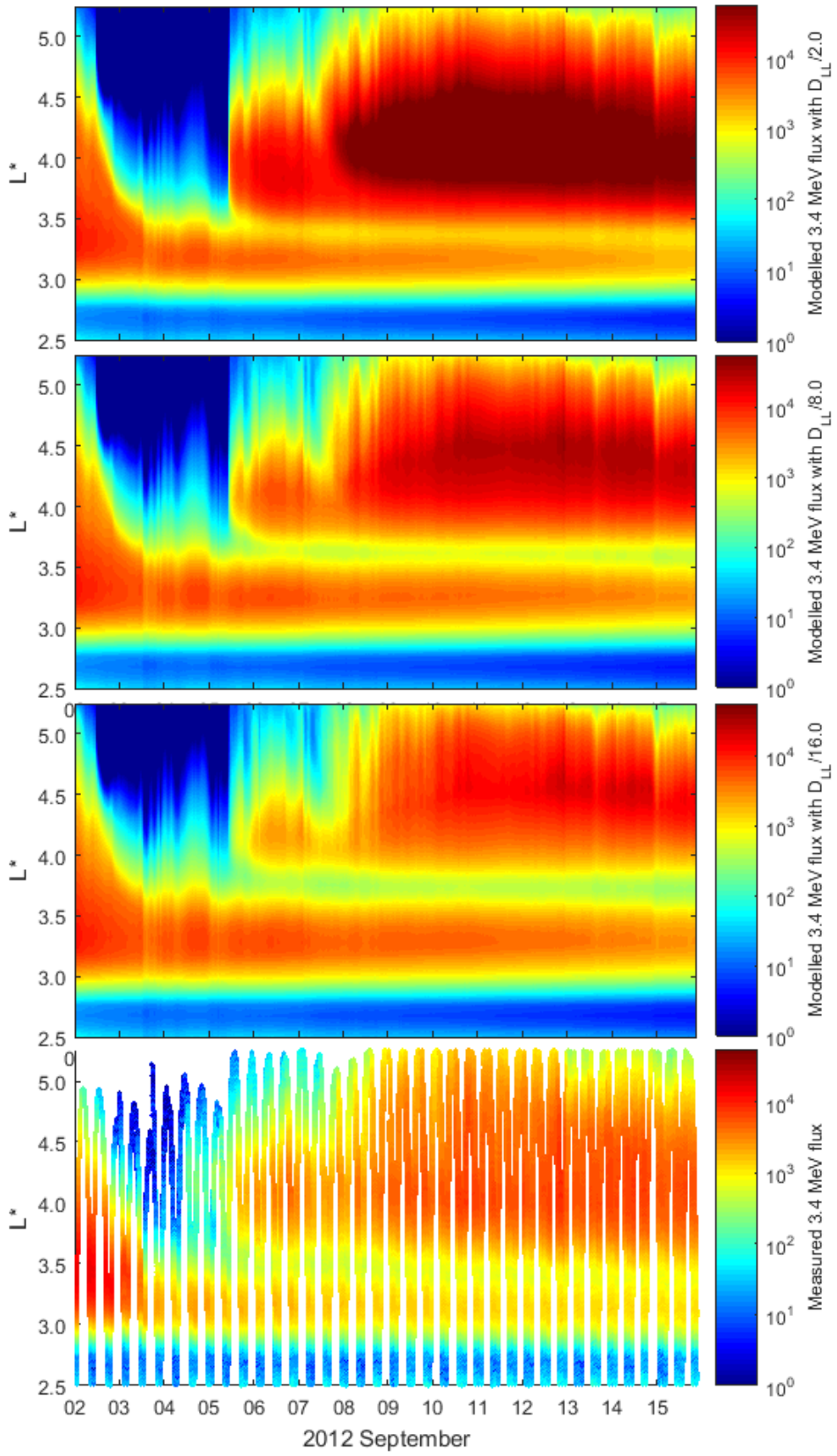

Extended Data Fig. 4. Simulations of the 3.4 MeV electron flux when the overall radial diffusion coefficient is reduced by a factor of 2 (top panel), 8 (second panel), 16 (third panel), as compared to the Van Allen Probe observed spin-averaged flux (bottom panel). The third panel contains the simulation parameters used in the middle panel of Figure 2 of the main article, and the effects of slow empirical hiss and chorus loss are included in all three simulations.

Extended Data Figure 5

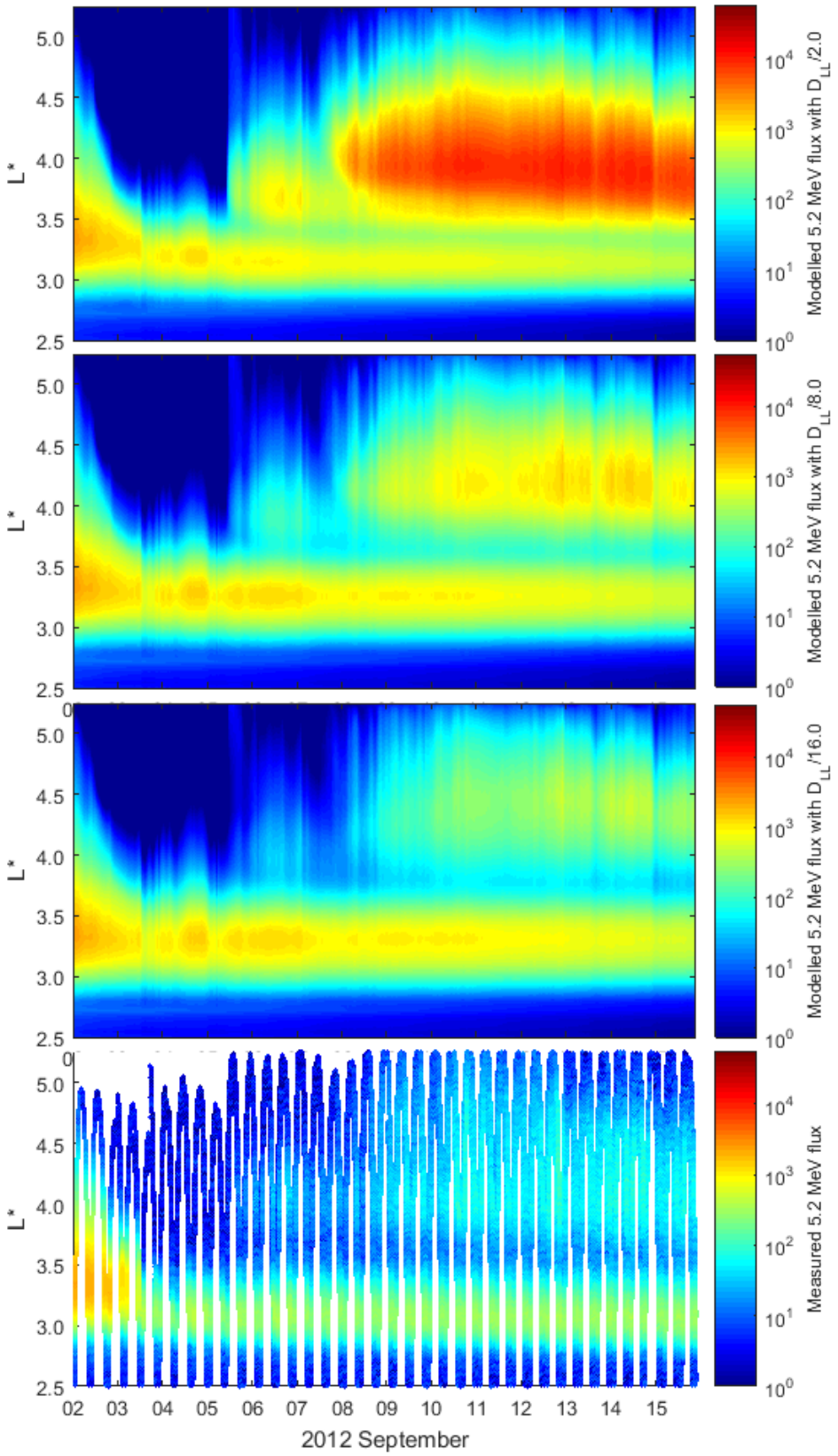

Extended Data Fig. 5. Same format as Extended Data Fig. 4 for 5.2 MeV energy channel. The third panel contains the simulation parameters used in the middle panel of Figure 3 of the main article.

Extended Data Figure 6.

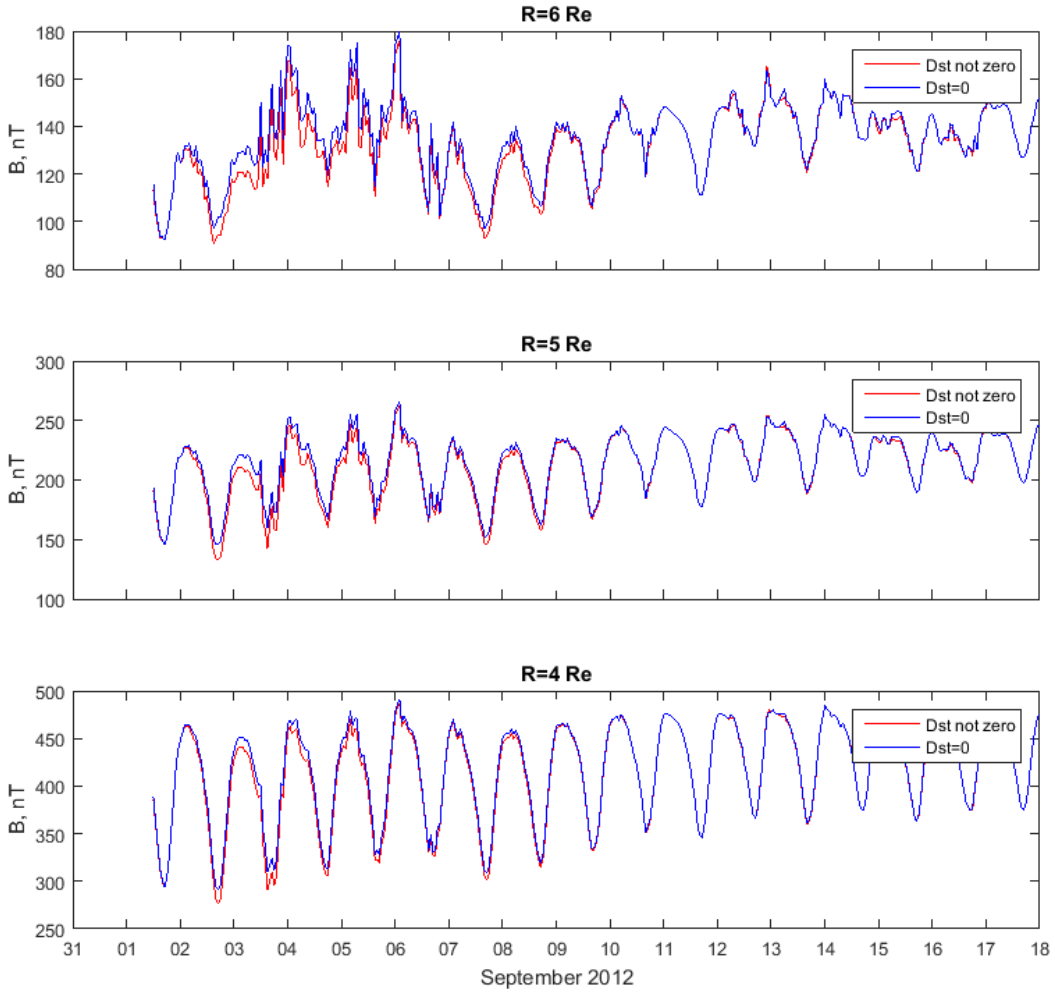

Extended Data Fig. 6. The effects of Dst on the magnetic field strength in the sub-solar meridian in the Tsyganenko (TS04D) magnetic field model. Magnetic field magnitude is plotted as a function of time in the equatorial plane (region of minimum magnetic field strength) mapped along field lines connected to the point (X, 0, 0) in the Geocentric Solar-Magnetospheric (GSM) coordinate system. Each panels shows field magnitude for the case (top) X=6, (middle) X=5, and (bottom) X=4 Earth Radius (Re). In each panel the magnetic field strength using the observed storm-time disturbance index Dst (red) as well as with the Dst set to zero (blue) are shown.